Localized cerebral blood flow response at submillimeter columnar resolution

Timothy Q. Duong, Dae-Shik Kim, Kâmil Uğurbil, and Seong-Gi Kim*

Center for Magnetic Resonance Research, Departments of Radiology and Neuroscience, University of Minnesota School of Medicine, Minneapolis, MN 55455

Edited by Marcus E. Raichle, Washington University School of Medicine, St. Louis, MO, and approved July 13, 2001 (received for review February 28, 2001)

Functional magnetic resonance imaging (fMRI) has been widely used for imaging brain functions. However, the extent of the fMRI hemodynamic response around the active sites, at submillimeter resolution, remains poorly understood and controversial. With the use of perfusion-based fMRI, we evaluated the hemodynamic response in the cat visual cortex after orientation-specific stimuli. Activation maps obtained by using cerebral blood flow fMRI measurements were predominantly devoid of large draining vein contamination and reproducible at columnar resolution. Stimulus-specific cerebral blood flow responses were spatially localized to individual cortical columns, and columnar layouts were resolved. The periodic spacing of orientation columnar structures was estimated to be 1.1 ± 0.2 mm (n = 14 orientations, five animals), consistent with previous findings. The estimated cerebral blood flow response at full width at half-maximum was 470 μm under single-stimulus conditions without differential subtraction. These results suggest that hemodynamic-based fMRI can indeed be used to map individual functional columns if large-vessel contributions can be minimized or eliminated.

The discovery by Roy and Sherrington (1) that regional cerebral blood flow (CBF) modulations are intricately coupled to changes in neuronal activity established the cornerstone for many modern functional brain-imaging modalities, including positron emission tomography (2) and functional magnetic resonance imaging (fMRI) (3–5). The latter has the capability to visualize brain functions noninvasively at system level with unprecedented spatiotemporal resolution. Whole-brain functional imaging with spatial resolution of a few millimeters to a centimeter can be readily achieved. With growing interest in obtaining improved spatial resolution and specificity, assessment of the intrinsic hemodynamic response function in the mammalian cortex becomes imperative, because the spatial extent of the hemodynamic response ultimately will impose a fundamental limitation on the spatial resolution of fMRI modalities. To date, however, the response function of the stimulus-evoked hemodynamic response remains poorly understood (6, 7). More importantly, it is uncertain whether the stimulus-evoked fMRI hemodynamic responses are sufficiently localized to the actual areas of elevated neuronal activity to resolve submillimeter functional units of the cortex (8, 9), such as cortical orientation columns.

It has been well documented that stimulus-induced metabolic increases are localized to individual orientation columns (10) that are separated by 1.1–1.4 mm, as demonstrated by the 2-deoxyglucose mapping technique. Intrinsic optical imaging (11, 12) showed that the initial increase of "metabolism-based" deoxyhemoglobin signal can also be used to resolve functionally active, individual orientation columns in the cat visual cortex. In marked contrast, the delayed elevation in oxyhemoglobin signals, resulting from stimulus-evoked CBF and blood volume increases, was spatially diffuse and extended far beyond the true activation site (12, 13). On the basis of these findings, it was concluded that the delayed oxyhemoglobin signal increase is less suited for resolving the columnar layouts. A similar conclusion was reached by using the blood oxygenation level-dependent (BOLD) fMRI technique (14, 15), which reflects deoxyhemoglobin content. The initial decrease in the BOLD response (often referred to as "dip"), presumably arising from the rapid onset of oxygen consumption increase, was more spatially confined to the site of increased neuronal activity, sufficient to resolve individual iso-orientation columns (14, 15). The delayed positive BOLD response, resulting from stimulus-evoked CBF increase and consequent decrease in deoxyhemoglobin content, seemed diffuse and less suitable for resolving the columnar layouts (14, 15).

The delayed optical signals associated with elevated oxyhemoglobin level and the delayed positive BOLD mapping signals were particularly sensitive to large draining vessels (16–20), which naturally lack spatial specificity. Therefore, it remains unclear whether the poor spatial specificity in the delayed optical and positive BOLD signals is caused by intrinsic properties of coupling between neuronal activity and blood flow, or alternatively, contamination from large draining veins as the stimulus-induced oxy- and/or deoxyhemoglobin changes propagate "downstream" because of blood flow. To address this question, pure CBF change at tissue level without large-vessel contribution (i.e., perfusion) has to be measured. Although less widely used than the BOLD technique because of its relatively poor temporal resolution (on the order of 1–6 s in comparison with subsecond resolution for BOLD), CBF-based fMRI can be targeted to tissue and small vessels (i.e., capillaries) avoiding large draining vein contributions (4, 21–23). In this study, we have used a perfusion-based, flow-sensitive alternating inversion recovery (FAIR) fMRI technique (22) to obtain functional maps based on local perfusion contrast only. We applied this approach to evaluate the response function of perfusion increases under a single-stimulus condition, and to determine whether the perfusion-based fMRI technique can be used to resolve columnar layouts. This study was performed on the well established cat model in which the spatial layouts of orientation columns have been well characterized with single-unit recordings (9), 2-deoxyglucose (10), optical imaging (12, 13), and early-negative BOLD fMRI (14, 15).

Methods

Animal Preparations. All animal experiments were performed with institutional approval with use of a protocol detailed elsewhere (14, 15). Five female adolescent cats (0.5–1.1 kg) were treated with atropine sulfate (0.05 mg/kg, i.m.) and initially anesthetized with a ketamine (10–25 mg/kg) and xylazine (2.5 mg/kg) mixture (i.m.). After oral intubation, the animal was mechanically ventilated with a Harvard ventilator (≈35–45 strokes per min, 15–30 ml per stroke) under isoflurane anesthesia (1.0–1.3% vol/vol) in a 70:30 N_2O/O_2 mixture. End-tidal

This paper was submitted directly (Track II) to the PNAS office.

Abbreviations: fMRI, functional magnetic resonance imaging; CBF, cerebral blood flow; BOLD, blood oxygenation level dependent; FAIR, flow-sensitive alternating inversion recovery.

*To whom reprint requests should be addressed. E-mail: kim@cmrr.umn.edu.

The publication costs of this article were defrayed in part by page charge payment. This article must therefore be hereby marked "*advertisement*" in accordance with 18 U.S.C. §1734 solely to indicate this fact.

 www.pnas.org/cgi/doi/10.1073/pnas.191101098

CO_2 was kept at physiological level (3.4–4.0%). The animal was immobilized in the normal postural position with a head-holder, consisting of ear-and-mouth bars. Corrective eye contact lenses were used. The animal's rectal temperature was maintained at 38 ± 1°C.

Stimulation Paradigm. The stimulation paradigm used in this study was essentially identical with that used in optical imaging (12, 13) and BOLD fMRI studies (14, 15). Visual stimuli (presented to both eyes) consisted of high-contrast, moving square-wave gratings (0.15 cycle per degree, 2 cycles per s) of four different orientations (0°, 45°, 90°, and 135°). Stationary gratings of identical spatial frequency and orientation were presented during the resting period. The visual stimuli were projected onto a screen from the back of the magnet by using a video projector. The screen was positioned ≈15 cm from the animal's eyes, covering about 37° of the visual field.

Magnetic Resonance Experiments. Magnetic resonance experiments were performed on a 4.7-T/40-cm horizontal magnet (Oxford Magnet Technology, Oxford, UK), equipped with a home-built 15-G/cm gradient (300-μs risetime, i.d. = 11 cm) and an INOVA console (Varian). After placing the animal in a cradle, a small surface coil of 1.6-cm (inner) diameter was placed on top of the cat brain. A single oblique slice, ≈500 μm below the cortical surface, was chosen to target the columnar structure in area 18 with minimal superficial vessel contamination as demonstrated (14).

CBF fMRI measurements were made with use of the FAIR technique (22). Paired images were acquired alternately, one with slice-selective inversion and the other non-slice-selective inversion. Single-shot, gradient-echo echo-planar images were acquired with the following parameters: repetition time (*TR*), 3.0 s; inversion delay (*TI*), 1.5 s; echo time (*TE*), 31 ms; data matrix, 64 × 64; field of view, 2 × 2 cm^2; slice thickness, 2 mm; and flip angle, 90°. A 10-ms adiabatic full-passage (hyperbolic secant) pulse was used for slice inversion. The slice-selective inversion slab was 5 mm thick. Seventy pairs of images were acquired during a three-epoch stimulus paradigm of 10-**10**-10-**10**-10-**10**-10 image pairs. (Bold cases indicated moving grating stimulus conditions for 60 s each.) Ten to 20 repeated CBF fMRI measurements were performed for each orientation stimulus.

In two of the five animals, additional gradient-echo BOLD measurements were performed on the same imaging slice as described in detail elsewhere (14). The parameters were essentially identical with the CBF measurement, except *TR* = 0.5 s, flip angle = 60°, and no inversion pulse was used. For each BOLD fMRI measurement, 160 images were acquired, with 60 images prestimulation, 20 images during stimulation, and 80 images poststimulation. Typically, 5–10 repeated BOLD fMRI measurements were made for each orientation stimulus.

Data Analysis. Single-condition maps, reproducibility of the CBF maps, cluster spacings, full-width-at-half-maximum of the CBF fMRI responses, complementarity of orthogonal maps, and comparison of CBF and early-negative BOLD maps were analyzed. In two animals, data from four orientations were successfully acquired, whereas in the remaining three animals, data from only two orthogonal orientations were successfully obtained. Thus, there were seven pairs of orthogonal orientation data sets. For CBF and early-negative BOLD comparison, four single-orientation data sets in two animals were successfully acquired.

Repeated BOLD and CBF measurements of the same orientation stimulus were averaged and zero-filled from a data matrix of 64 × 64 to 256 × 256 before analysis. All image analysis used software codes written in PV-WAVE (Visual Numeric, Houston) and/or STIMULATE (24). Ghost artifact was minimal. No physiological correction or spatial and temporal filtering was applied. Unless otherwise specified, all reported values are in mean ± SD.

CBF images were obtained by pair-wise, pixel-by-pixel subtraction of the slice-selective images from the non-slice-selective images. *t* value CBF and BOLD activation maps ('single-condition' maps) were computed by comparing the experimental fMRI time course with the stimulation paradigm on a pixel-by-pixel basis. The activation maps were overlaid on inversion-recovery echo-planar images.

Reproducibility of the CBF map was obtained by comparing two sets of maps under repeated measures. Repeated CBF fMRI measurements were separated into two groups, with each group typically consisting of 5–10 scans. Two CBF maps were calculated typically with the same fixed *t* value threshold with the average *t* value of 0.9 ± 0.3 across subjects. This threshold yielded 40 ± 3% of area 18 to be "active." Reproducibility between the two maps was expressed as the percentage of overlap of the average activated pixels in the entire area 18, typically covering 6 × 6 mm^2.

Cluster size and spacing were determined by autocorrelation analysis of the CBF *t* value maps with use of the NIH IMAGE software (SCION, Frederick, MD). Autocorrelation analysis was computed for a 5 × 5 mm^2 (64 × 64 pixels) region of interest in area 18. Because the autocorrelation map is not radially symmetric, four radial profiles were sampled for each autocorrelation map to obtain an average profile. The average spacing between neighboring clusters was measured as the distance between the center peak and the next neighbor peak of the autocorrelation profile. The point spread was estimated by taking the full width at half-maximum of the center peak of the autocorrelation profile.

Spatial complementarity of two orthogonal orientations (i.e., 0° vs. 90° and 45° vs. 135°) was tested under single-stimulus conditions without use of differential subtraction. Orthogonal orientation maps were presented visually. The degree of complementarity was also estimated by computing the pixel-by-pixel correlation coefficient between the two orthogonal maps over a region of interest of ≈3.5 × 3.5 mm^2 by using a standard algorithm (25). To estimate the functional contrast of CBF changes between "active" and "inactive" columns, a time course was generated from active pixels in the entire area 18 for a given orientation stimulus (i.e., 0°) and the same pixels were used to obtain the time course during its orthogonal orientation stimulation (i.e., 90°).

Comparison between CBF and early-negative BOLD map from the same animals was presented visually, and correlation coefficients between the two maps were computed for a region of interest of ≈5 × 5 mm^2 with use of a standard algorithm (25). Additionally, representative one-dimensional spatial profiles (single-pixel strips) from the *t* value maps were obtained, and *t* values were plotted as a function of pixel position. One-dimensional spatial profiles were compared among CBF, early-negative, and delayed-positive BOLD maps on the same animals.

Results

Consistent and robust stimulus-evoked CBF responses were observed in essentially all repeated measures and all fMRI scans and studies (>95%). Comparison of CBF measurements between animals *in vivo* and *in vitro* (n = 4) demonstrated that the FAIR signals predominantly (>90%) reflected true blood flow. Control fMRI experiments, in which only stationary gratings were presented, showed no statistically significant activated pixels.

Fig. 1 *a–c* shows three representative CBF activation (*t* value) maps of the cat visual cortex obtained from three different animals during visual presentation of a single orientation stimulus. The drifting stimulus evoked a CBF response in area 18 of the visual cortex. Increased CBF activity was observed predom-

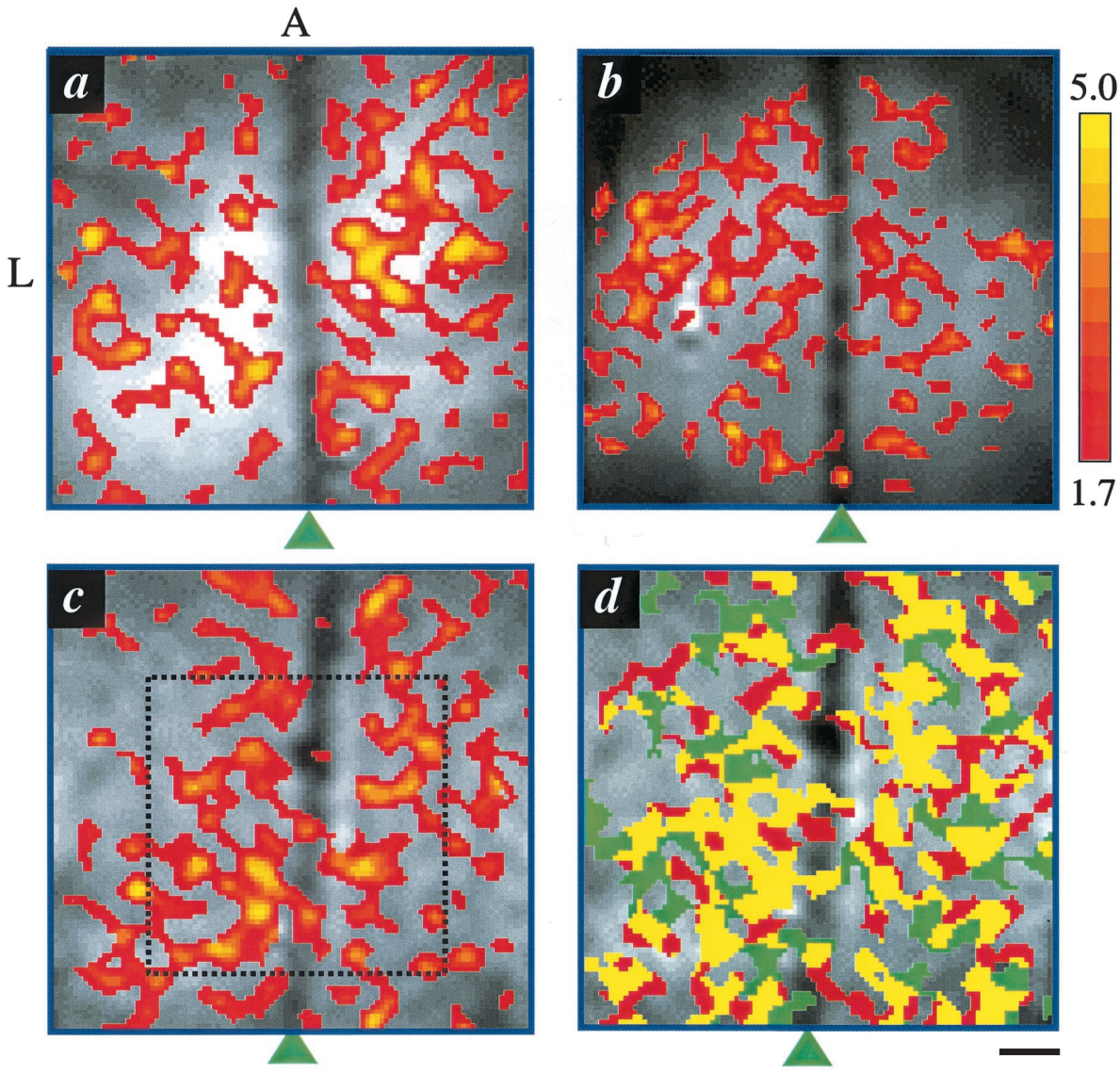

Fig. 1. (*a–c*) Representative single-condition, CBF functional maps of three cats overlaid on anatomical images. The colored bar shows the scale of the *t* values. Arrowheads indicate the positions of the midline. A 5 × 5-mm^2 (64 × 64 pixels) region of interest shown in *c* was used for auto correlation analysis in Fig. 2. (*d*) Reproducibility of CBF functional maps. Ten repeated CBF fMRI measurements of a single-orientation stimulus were grouped into two sets: the first and the last five. The yellow color designates the pixels that belong to both sets. Pixels that are active only in one set are shown as red or green. A, anterior; L, left. (Scale bar = 1 mm.)

inantly in the tissue area, avoiding the superior sagittal sinus. In some activation maps, a few activated pixels were observed along the sinus, likely originated from cortical tissues underneath the sinus, although a few pixels could arise from random noise fluctuation. No significant negative CBF activation was observed at this threshold. Most importantly, the CBF functional maps exhibit "patchy" layouts with semiregular cluster shapes, a prominent topological characteristic of orientation columns as observed by using 2-deoxyglucose (10), optical imaging (12, 13), and the early-negative BOLD techniques (14, 15). The semiregular cluster shapes are in marked contrast to the delayed positive BOLD response where large draining vessels were heavily labeled and the mapping signals seemed too diffuse for resolving the "patchy" layouts as demonstrated elsewhere (14, 15). CBF functional maps at columnar resolution were highly reproducible under repeated measures. The common (yellow) pixels between the two sets of functional maps under repeated measurements constituted 72% (68 ± 3, 14 orientations, five animals) of the average number of activated pixels (Fig. 1*d*). The overlapped pixels caused by chance, as obtained in the noise regions of the image outside the brain, were ≈6%.

Cluster spacings and cluster sizes were estimated by using autocorrelation analysis. Fig. 2 shows a two-dimensional autocorrelation map, a surface plot, and a horizontal trace across the autocorrelation map. This profile shows a clear periodicity. Note that the two-dimensional autocorrelation map is not radially symmetric, suggesting that the columnar clusters are asymmetrically spaced. The spacing across four radial projections of this autocorrelation map was 1.0 mm (1.1 ± 0.2 mm, n = 14), consistent with those obtained by using 2-deoxyglucose (10), "deoxyhemoglobin" optical imaging (26, 27) (1.1–1.4 mm), and early-negative BOLD (14, 15) (1.3 ± 0.2 mm). The average full width at half-maximum of the pixel clusters of this CBF map was estimated to be 460 μm (472 ± 74 μm, n = 14). As a control,

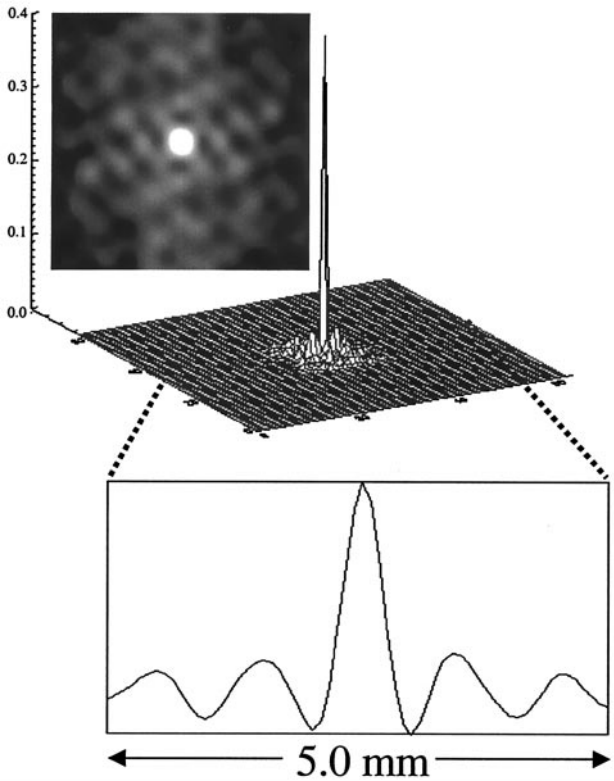

Fig. 2. Representative autocorrelation analysis of CBF *t* value map. A surface plot, a two-dimensional image of the autocorrelation map, and a horizontal profile across the autocorrelation map are shown. The periodic patterns in the autocorrelation suggest the presence of structured information. The columnar spacing (distance between the center peak and its neighboring peak) was estimated to be 1.0 mm, and the full width at half-maximum (of the center peak) of the columnar clusters was estimated to be 460 μm.

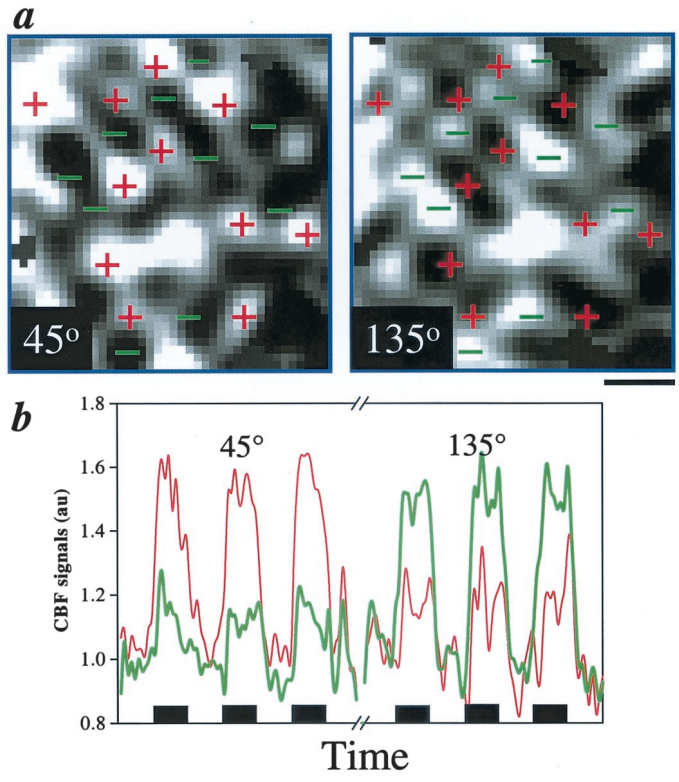

Fig. 3. (*a*) Complementarity of orthogonal 45° and 135° maps (no threshold). CBF-activated (bright) pixel clusters of the 45° stimulus were marked with + signs. These + signs in red were superimposed on the orthogonal 135° map. Similarly, CBF-activated (bright) pixel clusters of the 135° stimulus were marked with − signs in green. These − signs were superimposed on the orthogonal 45° map. (Scale bar = 1 mm.) (*b*) Time courses of orthogonal orientation maps. The thin red trace on the left shows a CBF time course of the activated pixels during the 45° stimulus. The thin red trace on the right shows a time course from the same pixels during 135° stimulation. Similarly, the thick green trace on the right shows a CBF time course of the activated pixels during the 135° stimulus, and that on the left shows a time course from the same pixels during 45° stimulation. Each black box under time courses indicates 1-min visual stimulation.

autocorrelation maps in the noise regions of the CBF maps were also analyzed; no prominent periodic structures were observed (data not shown).

Complementarity of orthogonal orientation stimuli was evaluated to elaborate on the veracity of the CBF-based single-condition columnar maps. Based on optical imaging (26) and 2-deoxyglucose (10) studies, functional columns responding to two orthogonal stimuli should approximately occupy complementary domains. Fig. 3 shows the results of the complementary test. The patchy clusters from orthogonal orientations occupy complementary cortical territories (Fig. 3*a*). Pixel-by-pixel correlation analysis showed that the "complementarity" between orthogonal maps was statistically significant in 4 of 7 possible pairs of orthogonal orientation data sets (average $r = -0.22$, $t = -10$, $P \ll 0.005$, $n = 4$). The CBF time courses between "active" and "inactive" columns also showed functional contrast (Fig. 3*b*). A marked CBF increase (55%) from the activated pixels during the 45° stimulus (*Left*, thin red trace) was observed, whereas the same pixels during the orthogonal 135° stimulus (*Right*) show a significantly smaller CBF increase (18%). Similarly, the activated pixels during the 135° stimulus (*Right*, thick green trace) show a marked CBF increase (51%), whereas the same pixels during the orthogonal 45° stimulus (*Left*) show a significantly smaller CBF increase (18%). CBF contrasts between the "active" and "inactive" pixel clusters were observed consistently, with clusters representing the "active columns" always showing a larger CBF change than the "inactive" ones. The average CBF percentage-change ratio of the "active" to "inactive" columns was 3.3 ± 0.6 ($n = 4$).

Fig. 4*a* shows the comparison of the spatial layouts between CBF and early-negative BOLD map from a representative animal during a single-orientation stimulus. The areas of increased CBF activity are generally in good agreement with those of increased early-negative BOLD activity. Pixel-by-pixel comparison indicates that the positive *t* value pixels of the CBF map significantly correlated with the negative *t* value of the early-negative BOLD map in 3 of 4 data sets (average $r = -0.20$, $t = -13$, $P \ll 0.005$, $n = 3$). The overlap was not perfect, presumably because of the differences in the contrast-to-noise ratio of the two measurements (early-negative BOLD signal has a poorer contrast-to-noise ratio) and/or variations across different measurements. Comparisons of the CBF, early-negative BOLD, and the delayed-positive BOLD response functions are shown in Fig. 4*b*. The spatial profiles of the CBF and early-negative BOLD signals show that cluster structures are well resolved, indicating that the CBF and early-negative BOLD responses are sufficiently localized for columnar resolution. On the contrary, the spatial profiles of the delayed-positive BOLD signals are relatively more diffuse, probably because of a draining vein contribution and/or distortion around large vessels.

Discussion

The major conclusion of this study is that stimulus-evoked CBF response is spatially confined to individual submillimeter cortical

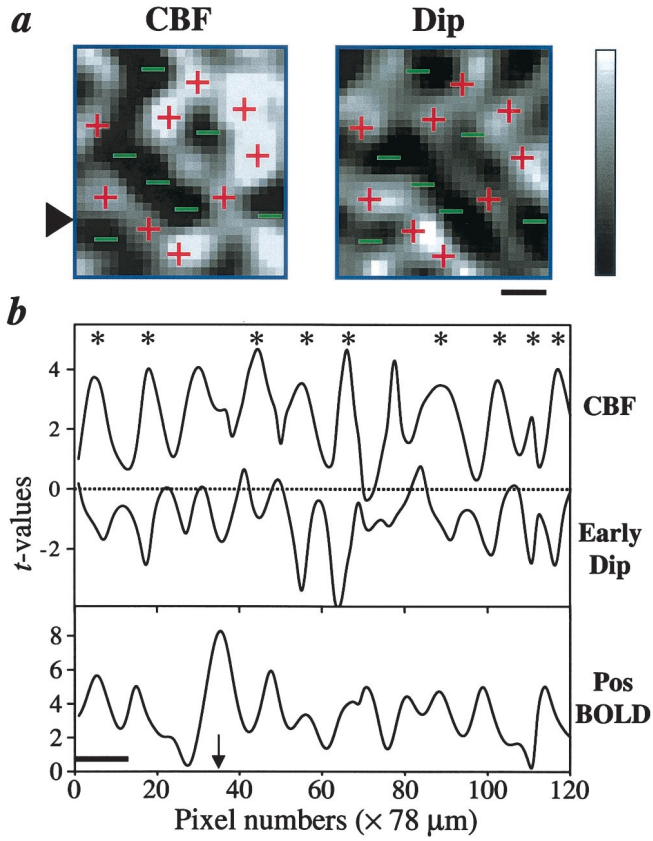

Fig. 4. (*a*) Comparison of CBF and early-negative *t* value maps (no statistical threshold). The + signs show areas of large signal changes from the CBF map, whereas − signs show areas with small signal changes. The gray-scale bar indicates the *t* values, which range from 0 to 4 for the CBF map, and from 0 to −4 for the dip map. (Scale bar = 1 mm.) (*b*) Spatial profiles of CBF, early-negative, and delayed-positive BOLD *t* value maps without statistical thresholds. The *t* values obtained from one single-pixel strip, obtained from the position indicated by the arrowhead in *a*, are plotted as a function of pixel position. The asterisks indicate the good spatial correlation between CBF and early-negative BOLD signals. Note that the strip profile was sampled across the sagittal sinus, but the map was obtained from a region away from the sinus. The arrow indicates the location of the sagittal sinus. (Scale bar = 1 mm.)

columns. This observation is inconsistant with previous findings based on optical imaging of cerebral blood volume (the sum of oxy- and deoxyhemoglobin optical signal) (12, 13) and the delayed-positive BOLD measurements (14, 15). These techniques, however, are susceptible to large draining vessel contamination. In particular, the delayed-positive, gradient-echo BOLD signal (as used for most conventional fMRI studies in humans) has contributions from both intra- and extravascular signals arising from large draining vessels. On the other hand, the perfusion-based signal change as measured by MRI (referred to as "FAIR" signal herein) is devoid of large draining vessel contamination (22). Further, FAIR contrast from the magnetically labeled, arterial water is also detected at the tissue level as well as at the arteriole/capillary level, because water can perfuse out of the capillaries and into the parenchyma. The CBF tissue contrast can be optimized by setting *TI* to tissue T_1 (tissue T_1 = 1.5–1.6 s at 4.7 T). Although a potential for draining vein contamination exists because of the long *TI* (relative to transit time), it is likely to be minimal because most of the labeled water is extracted into tissue and the remaining labeled water in blood loses most of its labeling by the time it reaches the draining veins. Therefore, the FAIR contrast predominantly arises from changes in local CBF at the level of arterioles and capillaries/tissues, as previously well documented (22, 28–30).

The point spread of the delayed-positive, gradient-echo BOLD signal in humans has been reported recently. In a visual cortex study, Engel *et al.* (6) demonstrated that the delayed-positive BOLD signal could be localized to ≈1.1 mm. By using the ocular dominance columns in humans as a model, Menon *et al.* (7) showed that the response function of the positive BOLD responses is ≈700 μm, but only after differential subtraction of the left and right eye responses. The differential subtraction method clearly cannot provide the *true* point spread, because it underestimates the spread of the BOLD response. In contrast, the CBF response as observed by using our FAIR method was obtained under single-stimulus conditions without differential subtraction. Our CBF response function is likely to be a rather "conservative" estimate, because the measured response (Fig. 2) is convoluted with the intrinsic point spread of our data sampling and the autocorrelation coefficient is not linear, which resulted in a slight overestimate, as verified by simulation. Nevertheless, the hemodynamic response could be different in different species, brain regions, and/or in the same brain regions but performing different tasks.

The most important implication of these results is that hemodynamic-based fMRI techniques *per se* can indeed be used to map individual functional columns *if* large-vessel contribution to the mapping signals can be minimized. Recent results from our group and other laboratories suggest that large-vessel contributions to fMRI signals can be reduced or eliminated through many different approaches. Those methods can be classified into three groups: (*i*) based on shorter stimulus duration, (*ii*) based on postprocessing techniques (7, 17–22, 31, 32), and (*iii*) based on improved data acquisition methods (14, 15, 33). A shorter (e.g., 2-s) stimulation duration has been proposed to minimize draining contamination, although it may not be entirely eliminated (12, 16). A common postprocessing technique used to minimize large-vessel contributions is the differential subtraction method. For example, the spread of positive (gradient-echo) BOLD signals can be sharpened through differential subtraction (7, 31, 32). However, such postprocessing methods cannot be applied to map most cortical functions, because their intrinsic orthogonal conditions are not known. An additional limitation of the differential subtraction method is that the extent and magnitude of BOLD signal changes induced by large draining vessels for two orthogonal stimuli have to be identical, which is not always true *a priori*.

It is therefore desirable to remove or minimize nonspecific large-vessel contribution through improved methods of data acquisition. Here, several alternative methods exist. First, the early portion of dip in BOLD signal can be used (14, 15, 34, 35). For example, this technique has been successfully applied for mapping columnar structures in anesthetized animals (14, 15). Nonetheless, this approach poses several challenges, because it yields a poor contrast-to-noise ratio (small percentage changes) and requires high spatial and temporal resolution. Consequently, the early dip has a small overall contrast-to-noise ratio and is highly susceptible to signal fluctuation of physiological origin (35). Second, spin-echo BOLD fMRI at high fields can be used (36). Here, extravascular BOLD signals from large vessels, which mostly arises from intravoxel dephasing, are largely eliminated by using a spin-echo acquisition scheme, whereas intravascular BOLD signals from large draining vessels are minimized by using high fields and/or by using flow-crushing bipolar gradients (33, 37, 38). However, sensitivity of this technique is strongly dependent on magnetic field. Both spin-echo and the early-dip BOLD techniques require high magnetic fields, because the BOLD signal at the capillary and tissue levels is very weak at low magnetic fields and is expected to increase quadratically with magnetic field strength (36).

Our current results suggest that the most robust approach to minimize large-vessel contributions in fMRI is a perfusion-based technique. Although the spatial specificity of the FAIR and the early-negative BOLD signals seem similar (Fig. 4*b*), the CBF responses demonstrate much improved contrast-to-noise ratio and reproducibility. Further, the CBF technique may be more versatile than both the early-negative BOLD and spin-echo BOLD techniques. Although there are some advantages of high magnetic fields in CBF-based measurements, such as the increased signal-to-noise ratio and half-life (long T_1) of the labeled spins, CBF change is independent of magnetic field strength and, thus, CBF-based fMRI can also be performed at low field. On the other hand, a drawback of the FAIR technique is its relatively poor temporal resolution. However, improvement in temporal resolution is possible with the use of the pseudocontinuous arterial labeling method (39) or by acquiring only spatially selective inversion recovery images if the BOLD contribution can be minimized. The latter can be accomplished by using spin-echo acquisition with a short echo time. Similarly, further improvement in the FAIR contrast is also expected by using a two-coil system: a large-volume coil for signal excitation and a small-surface coil for signal detection.

In conclusion, these results strongly suggest that the CBF change associated with increased neuronal activity is spatially localized to individual submillimeter columns. Because of its spatial specificity and robustness, perfusion-based fMRI can be a superior approach for noninvasive mapping of functional structures at submillimeter resolution compared with other existing noninvasive techniques. In particular, this approach can be of pivotal importance for future human fMRI studies at high spatial resolution.

We thank Drs. C. Iadecola and A. Shmuel for helpful suggestions and Dr. H. Merkle for hardware support. This work was supported in part by National Institutes of Health Grants RR08079, NS38295, NS40719, MH57180, and NS10930.

1. Roy, C. S. & Sherrington, C. S. (1890) *J. Physiol.* **1,** 85–108.
2. Raichle, M. E. (1987) in *Handbook of Physiology: The Nervous System*, ed. Plum F. (Am. Physiol. Soc., Bethesda), Vol. V, pp. 643–674.
3. Ogawa, S., Tank, D. W., Menon, R., Ellermann, J. M., Kim, S.-G., Merkle, H. & Ugurbil, K. (1992) *Proc. Natl. Acad. Sci. USA* **89,** 5951–5955.
4. Kwong, K. K., Belliveau, J. W., Chesler, D. A., Goldberg, I. E., Weisskoff, R. M., Poncelet, B. P., Kennedy, D. N., Hoppel, B. E., Cohen, M. S., Turner, R., *et al.* (1992) *Proc. Natl. Acad. Sci. USA* **89,** 5675–5679.
5. Bandettini, P. A., Wong, E. C., Hinks, R. S., Rikofsky, R. S. & Hyde, J. S. (1992) *Magn. Reson. Med.* **25,** 390–397.
6. Engel, A., Glover, G. & Wendel, B. (1997) *Cereb. Cortex* **7,** 181–192.
7. Menon, R. S. & Goodyear, B. G. (1999) *Magn. Reson. Med.* **41,** 230–235.
8. Mountcastle, V. B. (1957) *J. Neurophysiol.* **20,** 408–434.
9. Hubel, D. H. & Wiesel, T. N. (1962) *J. Physiol. (London)* **160,** 106–154.
10. Lowel, S. & Singer, W. (1988) *Exp. Brain Res.* **71,** 99–116.
11. Grinvald, A., Leike, E., Frostig, R. D., Gillbert, C. D. & Wiesel, T. N. (1986) *Nature (London)* **324,** 361–364.
12. Malonek, D. & Grinvald, A. (1996) *Science* **272,** 551–554.
13. Malonek, D., Dirnagl, U., Lindauer, U., Yamada, K., Kanno, I. & Grinvald, A. (1997) *Proc. Natl. Acad. Sci. USA* **94,** 14826–14831.
14. Duong, T. Q., Kim, D.-S., Ugurbil, K. & Kim, S.-G. (2000) *Magn. Reson. Med.* **44,** 231–242.
15. Kim, D.-S., Duong, T. Q. & Kim, S.-G. (2000) *Nat. Neurosci.* **3,** 164–169.
16. Grinvald, A., Slovin, H. & Vanzetta, I. (2000) *Nat. Neurosci.* **3,** 105–107.
17. Lai, S., Hopkins, A. L., Haacke, E. M., Li, D., Wasserman, B. A., Buckley, P., Friedman, H., Meltzer, H., Hedera, P. & Friedland, R. (1993) *Magn. Reson. Med.* **30,** 387–392.
18. Menon, R. S., Ogawa, S., Tank, D. W. & Ugurbil, K. (1993) *Magn. Reson. Med.* **30,** 380–386.
19. Kim, S.-G., Hendrich, K., Hu, X., Merkle, H. & Ugurbil, K. (1994) *NMR Biomed.* **7,** 69–74.
20. Frahm, J., Merboldt, K.-D., Hanicke, W., Kleinschmidt, A. & Boecker, H. (1994) *NMR Biomed.* **7,** 45–53.
21. Edelman, R. R., Siewert, B., Darby, D. G., Thangaraj, V., Nobre, A. C., Mesulam, M. M. & Warach, S. (1994) *Radiology* **192,** 513–520.
22. Kim, S.-G. (1995) *Magn. Reson. Med.* **34,** 293–301.
23. Detre, J. A., Leigh, J. S., Williams, D. A. & Koretsky, A. P. (1992) *Magn, Reson. Med.* **23,** 37–45.
24. Strupp, J. P. (1996) *NeuroImage* **3,** S607.
25. Press, W. H., Teukolsky, S. A., Vetterling, W. T. & Flannery, B. P. (1992) *Numerical Recipes in C* (Cambridge Univ. Press, Cambridge, U.K.).
26. Bonhoeffer, T. & Grinvald, A. (1993) *J. Neurosci.* **13,** 4157–4180.
27. Shmuel, A. & Grinvald, A. (1996) *J. Neurosci.* **16,** 6945–6964.
28. Kim, S.-G. & Tsekos, N. V. (1997) *Magn. Reson. Med.* **37,** 425–435.
29. Tsekos, N. V., Zhang, F., Merkle, H., Nagayama, M., Iadecola, C. & Kim, S.-G. (1998) *Magn. Reson. Med.* **39,** 564–573.
30. Zaini, M. R., Strother, S. C., Andersen, J. R., Liow, J.-S., Kjems, U., Tegeler, C. & Kim, S.-G. (1999) *Med. Phys.* **26,** 1559–1567.
31. Menon, R. S., Ogawa, S., Strupp, J. P. & Ugurbil, K. (1997) *J. Neurophysiol.* **77,** 2780–2787.
32. Cheng, K., Waggoner, R. A. & Tanaka, K. (1999) in *Soc. Neurosci. Abstr.* **25,** 1422.
33. Lee, S.-P., Silva, A. C., Ugurbil, K. & Kim, S.-G. (1999) *Magn. Reson. Med.* **42,** 919–928.
34. Menon, R. S., Ogawa, S., Hu, X., Strupp, J. P., Anderson, P. & Ugurbil, K. (1995) *Magn. Reson. Med.* **33,** 453–459.
35. Hu, X., Le, T. H. & Ugurbil, K. (1997) *Magn. Reson. Med.* **37,** 877–884.
36. Ogawa, S., Menon, R. S., Tank, D. W., Kim, S.-G., Merkle, H., Ellermann, J. M. & Ugurbil, K. (1993) *Biophys. J.* **64,** 800–812.
37. Song, A. W., Wong, E. C., Tan, S. G. & Hyde, J. S. (1996) *Magn. Reson. Med.* **35,** 155–158.
38. Boxerman, J. L., Bandettini, P. A., Kwong, K. K., Baker, J. R., Davis, T. L., Rosen, B. R. & Weisskoff, R. M. (1995) *Magn. Reson. Med.* **34,** 4–10.
39. Silva, A. C. & Kim, S.-G. (1999) *Magn. Reson. Med.* **42,** 425–429.